THE ASTROPHYSICAL JOURNAL, 336:77–92, 1989 January 1

A COMBINED OPTICAL/X-RAY STUDY OF THE GALAXY CLUSTER ABELL 2256[1]

DANIEL G. FABRICANT, STEPHEN M. KENT,[2] AND MICHAEL J. KURTZ[3]
Harvard-Smithsonian Center for Astrophysics
Received 1987 June 24; accepted 1988 June 23

ABSTRACT

The dynamics of Abell 2256 ($z = 0.06$) are investigated by combining X-ray observations of the intracluster gas with optical observations of the galaxy distribution and kinematics. We present magnitudes and positions for 172 galaxies and new redshifts for 75. Abell 2256 is similar to the Coma Cluster in its X-ray luminosity, mass, and galaxy density. Both the X-ray surface brightness and the galaxy surface density distributions exhibit an elliptical morphology. The radial galaxy distribution is steeper than the density profile of the X-ray–emitting gas, yet the galaxy velocity dispersion is higher than the equivalent value for the gas. Under the simplest assumptions that the galaxy velocity distribution is isotropic and the gas is isothermal, the galaxies and gas cannot be in hydrostatic equilibrium in a common gravitational potential. Self-consistent dynamical models can be constructed that are in agreement with the available X-ray and optical data; these models have the common features that the mass-to-light ratio increases with radius and that the galaxy orbits are anisotropic with a radial bias. We consider, in addition, the possibility that the high apparent line-of-sight galaxy velocity dispersion may be the result of substructure in the cluster, contamination by interloper galaxies, or an extremely flattened geometry. If any of the latter three situations pertained, there would be no need to invoke radially increasing mass-to-light ratios or anisotropic galaxy orbits.

Subject headings: galaxies: clustering — galaxies: intergalactic medium — galaxies: redshifts — X-rays: sources

I. INTRODUCTION

It has long been recognized that clusters of galaxies likely harbor large amounts of unseen matter, but the distribution of this matter is not well known. Interpretation of the density and velocity dispersion profiles of the galaxies is complicated by the unknown anisotropy in the velocity distribution (e.g., Kent and Gunn 1982; Kent and Sargent 1983; The and White 1986; Merritt 1987). In principle, X-ray observations of hot gas in clusters provide a better tool for determining the mass distribution, since this last degree of freedom is not present in gas. However, the gas temperature profiles in high-temperature clusters cannot yet be measured reliably, so at present X-ray observations provide only a different and independent set of constraints on the mass distribution. Determination of the mass-to-light (M/L) ratio as a function of radius in clusters is of great interest because, if the universe is critically bound, the M/L ratio of the universe as a whole must be larger than that of individual clusters by a factor of about 5. Clusters of galaxies may possess a "dark halo" in analogy with galaxies.

Abell 2256 is a rich, regular cluster at $z = 0.06$ with a smooth X-ray morphology. For these reasons, it was selected for detailed observation with the Imaging Proportional Counter (IPC) on the *Einstein Observatory* (Fabricant, Rybicki, and Gorenstein 1984, hereafter FRG). These observations permit the determination of the gas density profile to a linear radius a factor of 2 larger than is typically possible for other nearby clusters. Abell 2256 has also been observed by *Ariel 5* (Mitchell *et al.* 1979) and *OSO 8* (Mushotzky *et al.* 1978). Existing optical observations consist of a deep galaxy survey by Dressler (1976, 1978) of the central $25' \times 25'$ and redshifts for 14 galaxies (Faber and Dressler 1977). Oegerle, Hoessel, and Jewison (1987) have derived the luminosity function and mapped the galaxy distribution in an 80′ square region around the cluster. Because of the unique quality of the X-ray data for this cluster, we decided to obtain additional data to allow us to better study the galaxy distribution and kinematics. We have obtained positions and magnitudes for galaxies over an 83′ square region and measured 75 new redshifts, increasing the total number of galaxies with redshifts to 89.

The new optical data are collected in §§ II and III. Section IV presents a review of the X-ray observations. Section V summarizes the similarities between Abell 2256 and the Coma Cluster. In § VI the observations are fitted to dynamical models for the cluster. In § VII alternative explanations for the high galaxy velocity dispersion are considered. The conclusions are summarized in § VIII. We use a Hubble constant of 50 km s^{-1} Mpc^{-1} throughout; the scale of Abell 2256 is then 100 kpc arcmin^{-1}.

II. GALAXY DISTRIBUTION

a) Observations

To augment the deep but narrow galaxy survey of Dressler (1976, 1978), we have obtained calibrated PDS positions and photometry for 172 galaxies within a region 83′ square centered at $\alpha = 17^{h}7^{m}9$, $\delta = 78°39'9$ (about 5′ southeast of the cluster center). The photometry is derived from PDS scans of the KPNO glass copy of the Palomar Sky Survey plate E-1433. A 4000×4000 square raster of nonoverlapping 20 μm pixels was digitized and reduced to a list of galaxies by the methods described in Kurtz *et al.* (1985) and Fabricant *et al.* (1986). The scanned region is rotated by 7°3 from north to east. The magnitudes were converted to the r bandpass of Thuan and Gunn (1976) after calibration with a pair of CCD frames obtained

[1] Research reported here is based in part on observations made with the Multiple Mirror Telescope, a joint facility of the Smithsonian Institution and the University of Arizona.

[2] Presidential Young Investigator and Alfred P. Sloan Fellow.

[3] Visiting Scientist, Kitt Peak National Observatory.

with the Harvard 8″ (20 cm) telescope (Kent 1987). Magnitudes were measured within a limiting isophote $\mu = 24.5$ mag arcsec^{-2}. The rms error in the PDS-CCD magnitudes is 0.1 mag, and we conservatively apply this error to the reduced magnitudes. The final list of galaxies is given in Table 1; their positions are plotted in Figure 1. The sample is complete to a limiting magnitude $r = 16.8$.

Using the CCD frames, we also made an independent check of the (F) magnitudes derived by Dressler (1976) for galaxies in the central 25′ field. We find that for galaxies fainter than $r = 15.5$, there is a constant offset $r - F = 0.5$, but for brighter galaxies Dressler's magnitudes are apparently too faint by about 0.3 mag mag^{-1}.

b) Cluster Parameters

Sarazin (1980) has used a maximum-likelihood method to find the center and core radius of a galaxy distribution without the necessity of binning the data. We have extended his method to solve also for a mean flattening and major-axis position angle of the galaxy distribution. We use an *a priori* surface density profile $\mu = \mu_0(1 + x^2/a^2 + y^2/b^2)^{-1}$ and determine the axial ratio a/b, the mean core radius $r_c = (ab)^{1/2}$, the position angle θ, and the position of the cluster center. The density of background galaxies is kept fixed.

From our redshift data (§ III) we estimate that the background contamination is in the range 3–14 galaxies deg^{-2}. Independent estimates of the background density tend to be somewhat higher. Our limiting magnitude of $r = 16.8$ corresponds to $F = 16.3$ or $J = 17.3$. At these limiting magnitudes Dressler (1976) finds a background density of 16 galaxies deg^{-2}, and Butcher and Oemler (1985) find 18 galaxies deg^{-2}. To reflect the uncertainties in the background determination, we will use both 8 and 16 galaxies deg^{-2} in deriving the cluster parameters.

Two parameters are independent of the background density. The cluster center is $\alpha = 17^h6^m.6$, $\delta = 78°42'.9$ with an uncertainty of about 1′ in each coordinate, and the position angle is 114°. Using a background density of 8 galaxies deg^{-2}, we find $r_c = 4'.2^{+1.8}_{-1.4}$ and $a/b = 1.8^{+0.6}_{-0.5}$; with a background density of 16, we find $r_c = 3'.7^{+1.4}_{-1.3}$ and $a/b = 1.9^{+1.0}_{-0.6}$. These (90%) error bounds were determined by finding the contours of r_c and a/b which increased the function S [$= -2 \log$ (likelihood)] by 4.6 above S_{min} while simultaneously adjusting the other parameters to minimize S (Avni 1976). We have verified that the maximum-likelihood models provide an acceptable description of the data using a V'/V'_{max} test as described by Fabricant *et al.* (1986). As a semi-independent check on these parameters, we have also analyzed the narrower but much deeper survey of Dressler (1976, 1978). To a limiting magnitude $m_F = 18.5$ (the completeness limit of that survey), we find that, relative to our survey, the cluster center shifts east by $\sim 1'.5$ and south by $\sim 1'.0$, the core radius is $6'.5^{+2.8}_{-1.7}$, a/b is $2.3^{+1.3}_{-0.7}$ (at 90% confidence), and the position angle increases to 138°. From the same data set, but using different fitting techniques, Carter and

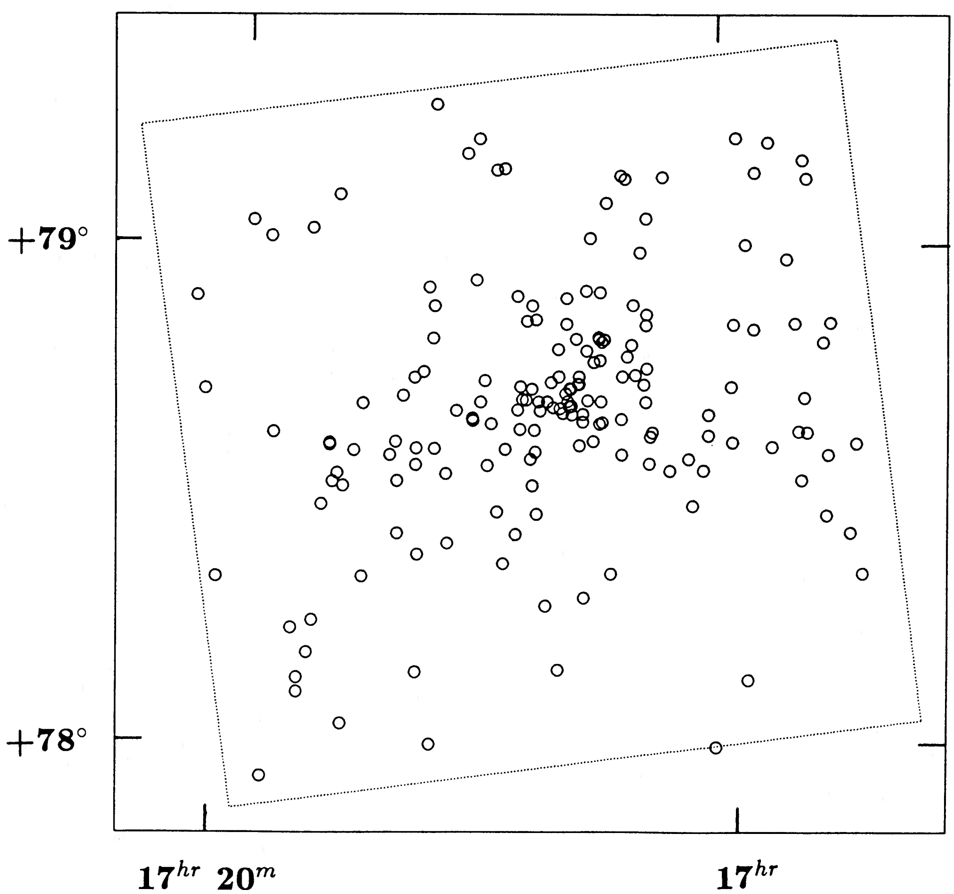

FIG. 1.—Space distribution of the 172 galaxies in our survey. A region 83′ on a side was surveyed; the boundary is marked by the dotted line. The magnitude limit is $m_r = 16.8$.

TABLE 1

Galaxy Data

Number	R.A. (1950)	Decl. (1950)	m_r	cz_h	1 σ Velocity Error	FD[a]	Dressler[b] Number
1	$16^h54^m53^s.4$	78°20′49″	16.11	...	...	...	...
2	16 54 53.6	78 36 36	15.97	...	...	...	...
3	16 55 17.8	78 25 52	15.76	...	...	...	...
4	16 55 42.8	78 51 14	16.77	...	...	...	...
5	16 56 02.0	78 35 22	15.40	...	...	...	...
6	16 56 02.5	78 48 53	15.63	...	...	...	...
7	17 56 12.1	78 28 08	15.16	...	...	...	...
8	16 56 27.8	79 08 48	15.25	...	...	...	...
9	16 56 35.1	79 11 00	16.34	...	...	...	...
10	16 56 51.1	78 38 10	16.66	...	...	...	...
11	16 56 54.2	78 42 20	14.86	...	...	...	...
12	16 57 08.3	78 32 28	15.52	...	...	...	...
13	16 57 09.9	78 51 18	15.76	...	...	...	...
14	16 57 11.4	78 38 18	14.72	...	...	...	...
15	16 57 24.5	78 59 10	16.59	...	...	...	...
16	16 58 01.6	79 13 18	15.33	...	...	...	...
17	16 58 16.7	78 36 34	16.16	...	...	...	...
18	16 58 37.7	79 09 41	14.91	...	...	...	...
19	16 58 51.9	78 50 45	16.05	...	...	...	
20	16 59 05.8	79 01 03	15.75	...	...	...	...
21	16 59 22.5	79 13 56	15.96	...	...	...	...
22	16 59 28.7	78 08 32	16.75	...	...	...	...
23	16 59 40.1	78 51 25	16.40	...	...	...	...
24	16 59 50.5	78 43 53	16.58	...	...	...	...
25	16 59 50.9	78 37 14	16.04	...	...	...	...
26	17 00 45.5	78 00 34	16.21	...	...	...	...
27	17 00 46.0	78 40 37	15.77	...	...	...	...
28	17 00 47.4	78 38 08	15.40	19,202	40	...	...
29	17 01 02.1	78 33 54	14.77	17,844	40	...	...
30	17 01 28.7	78 29 40	15.18	15,613	48	...	...
31	17 01 36.5	78 35 18	16.11	18,504	44	...	...
32	17 02 22.0	78 33 57	16.17	15,803	50	...	...
33	17 02 29.0	79 09 26	16.22	...	...	...	...
34	17 03 03.0	78 38 37	16.30	18,355	62	...	...
35	17 03 07.2	78 38 06	16.71	...	...	...	...
36	17 03 10.9	78 34 49	16.32	17,421	52	...	486
37	17 03 11.9	79 04 27	16.44	...	...	...	...
38	17 03 13.8	78 52 49	16.13	15,332	47	...	480
39	17 03 14.2	78 46 18	16.77	...	...	...	482
40	17 03 15.0	78 51 32	16.12	18,931	32	...	481
41	17 03 18.3	78 42 16	16.40	17,775	54	...	479
42	17 03 22.0	78 44 23	15.77	17,921	35	...	473
43	17 03 28.1	79 00 22	16.39	15,237	47	...	...
44	17 03 42.9	78 45 30	15.89	17,325	39	...	465
45	17 03 45.8	78 53 59	16.31	17,357	43	...	462
46	17 03 51.5	78 49 08	15.58	16,147	64	...	458
47	17 04 02.4	78 47 43	15.29	16,038	100	FD	453
48	17 04 03.8	79 09 17	16.58	...	...	...	...
49	17 04 14.3	78 45 22	15.73	16,217	67	...	445
50	17 04 14.6	79 09 39	16.18	...	...	...	...
51	17 04 17.1	78 35 58	16.69	...	...	...	443
52	17 04 18.3	78 40 14	16.16	18,092	47	...	440
53	17 04 45.7	78 21 34	15.55	18,001	47	...	...
54	17 04 51.9	79 06 22	13.79	...	...	...	...
55	17 04 58.5	78 49 49	15.78	17.770	46	...	411
56	17 05 03.7	78 39 50	15.64	18,362	100	FD	410
57	17 05 03.9	78 49 32	16.02	17,988	43	...	408
58	17 05 07.1	78 42 21	16.67	15,806	39	...	406
59	17 05 07.3	78 55 35	16.12	19,421	59	...	...
60	17 05 09.3	78 47 19	16.56	18,127	34	...	405
61	17 05 10.7	78 49 54	16.74	...	...	...	400
62	17 05 11.4	78 39 40	16.61	16,730	47	...	403
63	17 05 11.6	78 50 06	15.96	19,752	40	...	...

TABLE 1—*Continued*

Number	R.A. (1950)	Decl. (1950)	m_r	cz_h	1 σ Velocity Error	FD[a]	Dressler[b] Number
64	17 05 24.1	78 47 06	16.68	15,419	60	...	392
65	17 05 26.2	78 37 35	16.60	15,390	46	...	390
66	17 05 32.0	79 02 08	16.64	...	...	...	...
67	17 05 39.4	78 42 28	15.92	16,936	39	...	379
68	17 05 41.0	78 48 27	14.45	20,116	24	...	378
69	17 05 42.2	78 55 46	15.52	16,514	43	...	...
70	17 05 49.7	78 18 40	15.89	...	...	...	...
71	17 05 51.1	78 40 51	16.16	16,545	35	...	366
72	17 05 51.9	78 39 55	15.05	16,303	100	FD	364
73	17 05 59.8	78 37 06	16.42	16,718	39	...	353
74	17 06 01.1	78 45 19	16.74	...	...	...	352
75	17 06 02.4	78 44 27	16.31	15,901	39	...	351
76	17 06 02.9	78 44 17	17.80	16,637	52	...	350
77	17 06 07.4	78 49 55	16.65	15,660	39	...	345
78	17 06 18.4	78 40 48	16.71	...	...	...	334
79	17 06 18.5	78 41 46	14.00	17,584	100	FD	332
80	17 06 20.8	78 43 51	15.30	17,558	36	...	329
81	17 06 22.4	78 41 42	14.00	16,912	100	FD	327
82	17 06 24.0	78 43 54	16.57	15,479	35	...	322
83	17 06 25.1	78 41 42	14.00	15,830	100	FD	323
84	17 06 28.3	78 42 24	16.63	17,628	46	...	318
85	17 06 30.8	78 54 52	16.28	19,148	105	...	312
86	17 06 31.0	78 51 42	14.84	19,800	100	FD	320
87	17 06 33.6	78 43 17	16.66	...	...	...	309
88	17 06 40.6	78 40 58	16.75	...	...	...	304
89	17 06 46.9	78 41 31	16.16	15,164	47	...	298
90	17 06 50.1	78 45 21	16.50	20,404	46	...	294
91	17 06 50.5	78 48 39	15.80	17,138	37	...	296
92	17 06 50.6	78 10 02	15.78	...	...	...	...
93	17 07 03.9	78 41 37	13.92	16,903	100	FD	276
94	17 07 08.3	78 44 39	15.99	15,690	72	...	270
95	17 07 17.7	78 42 18	13.34	17,808	53	...	259
96	17 07 19.9	78 17 42	16.41	...	...	...	...
97	17 07 34.3	78 41 14	16.07	15,230	35	...	239
98	17 07 38.9	78 42 19	14.76	19,276	100	FD	234
99	17 07 42.6	78 28 50	16.49	26,961	40	...	223
100	17 07 44.5	78 52 13	15.44	19,717	47	...	225
101	17 07 45.5	78 36 16	16.75	...	...	...	217
102	17 07 48.6	78 38 55	16.77	...	...	...	216
103	17 07 52.4	78 32 13	15.65	19,367	38	...	208
104	17 07 54.3	78 53 57	16.27	19,590	52	...	212
105	17 07 55.1	78 43 52	16.40	16,762	49	...	206
106	17 07 57.6	78 35 25	16.36	16,547	45	...	201
107	17 08 07.1	78 52 03	16.72	...	...	...	199
108	17 08 09.0	78 42 33	16.55	17,682	47	...	188
109	17 08 18.5	78 42 36	16.25	19,599	57	...	176
110	17 08 22.7	78 44 07	16.20	17,194	65	...	174
111	17 08 23.2	78 39 00	15.27	18,746	100	FD	170
112	17 08 29.7	78 41 21	15.59	16,126	49	...	163
113	17 08 31.0	78 55 03	15.98	19,637	39	...	...
114	17 08 32.0	78 26 23	15.94	16,437	45	...	...
115	17 08 59.1	78 36 35	15.42	18,494	100	FD	135
116	17 09 00.9	78 22 49	16.70	...	...	...	...
117	17 09 07.0	79 10 29	15.74	...	...	...	...
118	17 09 16.3	78 29 04	15.61	15,626	35	...	123
119	17 09 25.6	79 10 19	16.43	...	...	...	...
120	17 09 32.7	78 39 38	16.72	...	...	...	109
121	17 09 40.5	78 34 38	16.15	17,998	61	...	97
122	17 09 49.2	78 44 51	15.60	16,865	46	...	94
123	17 09 59.3	78 42 15	15.80	18,873	44	...	82
124	17 10 11.1	79 14 01	16.43	...	...	...	...
125	17 10 12.7	78 56 59	15.93	16,680	35	...	...
126	17 10 16.8	78 40 00	16.47	17,574	54	...	65
127	17 10 17.8	78 40 19	16.32	17,783	42	...	58
128	17 10 39.8	79 12 16	15.49	...	...	...	...

TABLE 1—*Continued*

Number	R.A. (1950)	Decl. (1950)	m_r	cz_h	1 σ Velocity Error	FD[a]	Dressler[b] Number
129............	17 10 56.7	78 41 11	16.29	17,841	49	...	32
130............	17 11 12.3	78 25 14	16.02	21,683	35	...	...
131............	17 11 25.9	78 33 43	15.40	18,734	34	...	14
132............	17 11 44.1	78 00 58	15.78	...	...	...	...
133............	17 11 48.1	78 36 34	16.75	...	...	...	...
134............	17 11 55.3	78 53 46	15.57	16,047	50	...	...
135............	17 11 57.0	78 49 50	15.46	11,924	41	...	...
136............	17 12 01.0	79 18 05	15.86	...	...	...	...
137............	17 12 09.0	78 56 03	15.55	18,912	73	...	...
138............	17 12 18.0	78 45 48	16.39	17,956	77	...	...
139............	17 12 20.9	78 09 37	15.92	...	...	...	...
140............	17 12 24.0	78 23 48	15.12	17,184	55	...	...
141............	17 12 31.9	78 34 36	16.63	18,561	38	...	...
142............	17 12 32.4	78 36 35	15.73	16,148	46	...	...
143............	17 12 40.4	78 45 05	16.58	17,892	42	...	...
144............	17 13 06.3	78 42 52	16.44	17,043	53	...	...
145............	17 13 12.3	78 26 17	16.70	...	...	...	...
146............	17 13 16.5	78 32 36	16.54	15,908	53	...	...
147............	17 13 21.8	78 37 20	16.68	...	...	...	...
148............	17 13 35.4	78 35 43	15.11	18,767	31	...	...
149............	17 14 33.6	78 20 54	16.79	...	...	...	...
150............	17 14 44.1	78 41 49	16.67	...	...	...	...
151............	17 15 02.2	78 36 07	16.63	...	...	...	...
152............	17 15 09.8	78 03 10	16.34	...	...	...	...
153............	17 15 25.2	78 31 49	16.33	...	...	...	...
154............	17 15 40.3	78 33 20	16.67	...	...	...	...
155............	17 15 50.1	78 32 19	15.66	...	...	...	...
156............	17 15 58.4	79 06 56	16.37	...	...	...	...
157............	17 15 59.5	78 36 57	15.90	...	...	...	...
158............	17 15 59.7	78 36 43	14.95	...	...	...	...
159............	17 16 14.6	78 29 30	16.08	...	...	...	...
160............	17 16 25.9	78 15 27	16.16	...	...	...	...
161............	17 16 35.4	78 11 33	15.40	...	...	...	...
162............	17 16 54.0	78 06 46	16.15	...	...	...	...
163............	17 16 56.1	78 08 31	15.14	...	...	...	...
164............	17 17 01.9	79 02 45	14.87	...	...	...	...
165............	17 17 13.9	78 14 26	16.60	...	...	...	...
166............	17 18 07.9	77 56 31	16.70	...	...	...	...
167............	17 18 16.6	78 37 59	16.37	...	...	...	...
168............	17 18 44.8	79 01 37	16.63	...	...	...	...
169............	17 19 30.7	79 03 27	16.68	...	...	...	...
170............	17 20 14.8	78 20 12	16.32	...	...	...	...
171............	17 21 05.3	78 42 45	16.41	...	...	...	...
172............	17 21 38.4	78 53 57	15.29	...	...	...	...

[a] FD signifies measurement by Faber and Dressler 1977.
[b] Galaxy number from Dressler 1976.

Metcalfe (1980) find a/b between 2 and 3.3 and a position angle of $145° \pm 6°$, both errors at 68% confidence. We conclude that the cluster parameters derived from both surveys agree to within their respective errors.

c) *Surface Density Profile*

It will be convenient to have the galaxy distribution binned to form an average radial number density profile. Following Kent and Gunn (1982), this has been done by computing the number density in circular bins whose width is adjusted to keep the number of galaxies per bin approximately constant. We average in circular rather than elliptical bins because the cluster flattening and orientation are somewhat uncertain. Averaging an elliptical distribution in circular bins produces a profile very similar to the true profile scaled to a radius $r = (ab)^{1/2}$. We use an *a priori* core radius of 4′ and a cluster center of $\alpha = 17^h6^m.5$, $\delta = 78°42'$. The bin boundaries are spaced uniformly in the quantity ln $[1 + (r/r_c)^2]$. The densities are also corrected for resolution effects as explained by Kent and Gunn (1982). We use a background density of 8 galaxies deg^{-2} (the entries can be easily corrected to any other desired density). The profile is given in Table 2.

To provide a smooth approximation to the galaxy distribution, we have fitted a King model to the surface density profile, adjusting the core radius r_c and central projected number density μ_0. To restrict the number of free parameters, we use the same $W_0 = 8.5$ King model that was found by Kent and Gunn (1982) to match the dynamics of the Coma Cluster. We

TABLE 2

GALAXY SURFACE DENSITY PROFILE

Radius	μ^{a} (galaxies deg^{-2})
1'.8	2077
4.8	606
7.3	401
10.3	344
14.1	108
18.9	120
25.2	75
33.4	34

[a] With error ±23%.

find $r_c = 3'.8$, and $\mu_0 = 2290$ galaxies deg^{-2}. The 90% confidence limits on r_c are 2'.7–5'.0. The core radius determined from the maximum-likelihood fit above differs from the least-squares fit, partly because the data have been binned here and partly because the King model used here has a slightly more extended shape than the approximation used previously.

d) Optical Luminosity

Although our galaxy survey of Abell 2256 does not extend to a faint limiting magnitude, we have estimated the total luminosity in galaxies. Because the fit to the galaxy luminosity function is not well constrained by our data, we have used the luminosity function obtained by Davis and Huchra (1982) for the CfA redshift survey, assuming $B - r = 1$. After making k- and extinction corrections and subtracting background, we find a total r-band luminosity of 1.7×10^{13} $L_{\odot}$ within a (projected) radius of 20'. This figure is uncertain by approximately a factor of 2 because of the limits of our survey.

III. RADIAL VELOCITIES

a) Observations

We have measured new radial velocities for 75 galaxies (plus three that overlap existing redshifts). These galaxies were chosen by observing in order of increasing magnitude galaxies from the central 43' × 43' of our survey (not precisely centered on the cluster). The spectroscopic measurements are complete to $m_r = 16.7$.

The spectra were acquired with the photon-counting Reticon system on the Multiple Mirror Telescope (Latham 1979). The spectra cover the range 3900–6900 Å with a resolution of 8 Å. Exposure times were typically 20 minutes. The spectra were reduced to heliocentric velocities using the standard CfA reduction software (Tonry and Davis 1979). The typical error in a redshift is 50 km s^{-1}.

The final velocities are tabulated in Table 1. For reference, the velocities for 11 galaxies measured by Faber and Dressler (1977) (and not remeasured by us) are listed as well, with the designation FD. A comparison of the redshifts of three galaxies measured in common with Faber and Dressler shows no significant zero-point offset. Combining the two samples, we have redshifts for 89 galaxies.

b) Cluster Membership

The velocity histogram is plotted in Figure 2. Two obvious nonmembers at 11,924 and 26,961 km s^{-1} fall outside the range of the plot. One galaxy at 21,600 km s^{-1} lies slightly separated from the main velocity distribution; we will also delete it as a background object (see Fig. 3). Hence we are left with 86 apparent cluster members which lie between 15,000 and 21,000 km s^{-1}. The mean heliocentric velocity is $cz = 17{,}431 \pm 147$ km s^{-1}, and the raw dispersion is 1372^{+112}_{-89} km s^{-1} (both errors being at the 68% confidence level). The

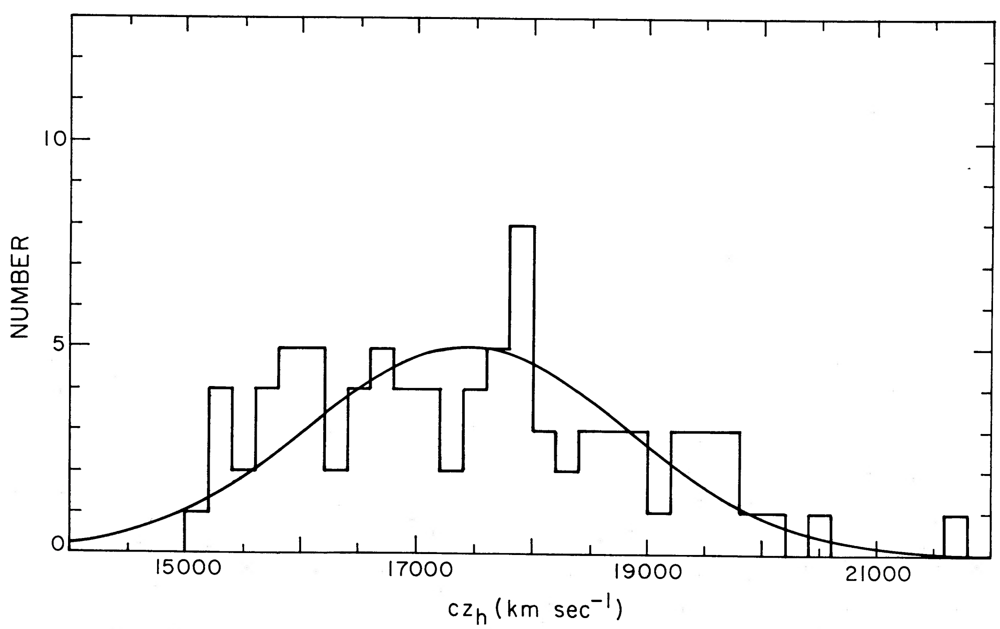

FIG. 2.—Velocity histogram of 87 galaxies with redshifts. Two obvious nonmembers fall outside the range of the plot. The single galaxy with $v = 21{,}683$ km s^{-1} is also probably not a member. A best-fitting Gaussian with mean 17,431 km s^{-1} and dispersion 1370 km s^{-1} is also plotted. The dispersion corrected for relativistic effects is 1300 km s^{-1}.

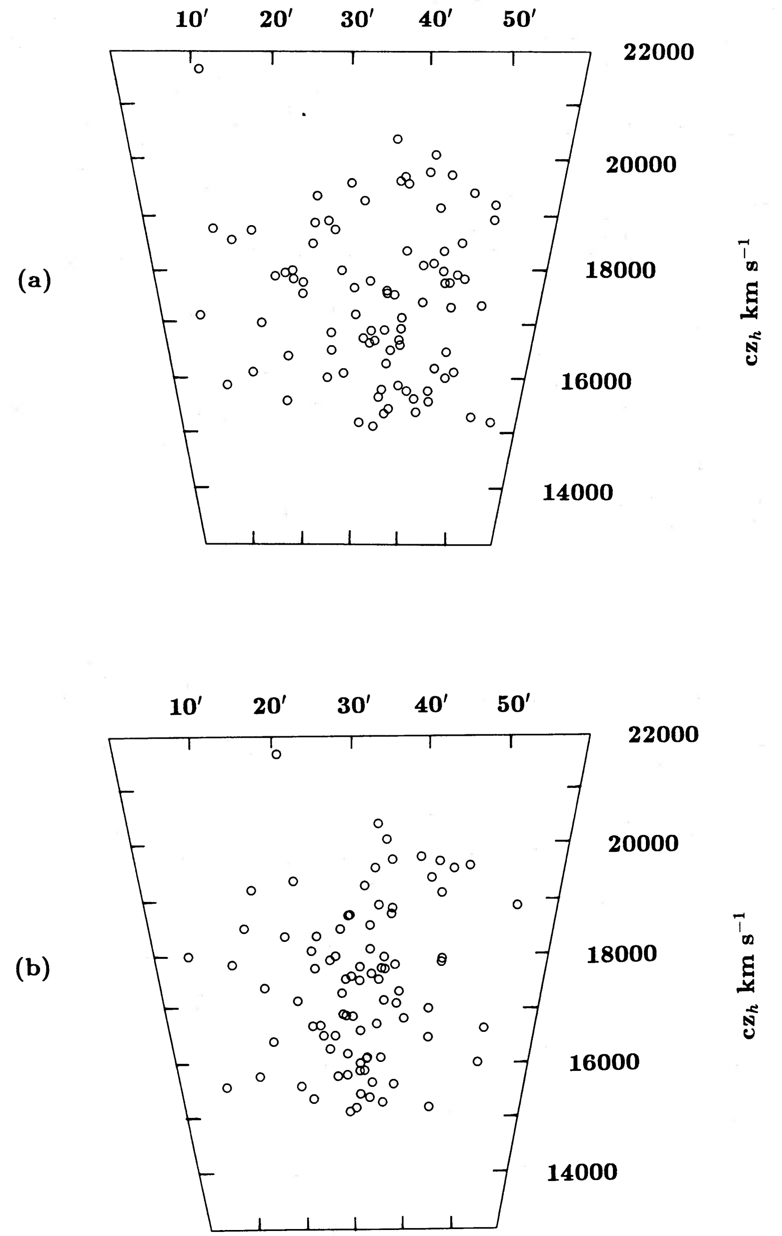

FIG. 3.—Cone diagrams of the 87 galaxies. The galaxies are shown (*a*) projected onto the major axis of the cluster (p.a. = 120°) and (*b*) projected onto the minor axis (p.a. = 30°). We have departed from the normal (and possibly misleading) practice of expanding the plot arbitrarily in polar coordinates; however, velocities have been plotted as though they represented distance.

true dispersion, corrected for relativistic effects, is 1300 km s^{-1} (Harrison 1974). A Gaussian function with these parameters is also shown in the figure. The velocity histogram appears to be rather flat and non-Gaussian. A Kolmogorov-Smirnov test reveals no significant deviations from a Gaussian. However, the "*a*" test (Pearson and Hartley 1976), which is sensitive to the kurtosis of the distribution, shows that the distribution is inconsistent with a Gaussian at the 96% confidence level. A non-Gaussian velocity distribution may be the result of an unusual velocity distribution function for the cluster, background contamination, or the presence of substructure. We shall return to this subject in §§ VI and VII.

With just 86 cluster members it is not possible to study the variation of velocity dispersion with radius in much detail. Table 3 gives the (relativistically corrected) velocity dispersion with the galaxies grouped into four radial bins. No peculiar behavior is seen, and the data are consistent with a constant dispersion at all radii.

TABLE 3

VELOCITY DISPERSION PROFILE

Radius	σ[a] (km s^{-1})
2′.2	1349
7.2	1237
12.7	1347
19.9	1223

[a] With error ±15%.

c) Background Contamination

Out of 89 galaxies in the central 43′ × 43′, we find that three are foreground or background galaxies. Hence for the entire sample of 104 galaxies we would expect to find 3.5 background objects, corresponding to a surface density of 6.8 galaxies $\deg^{-2}$. The uncertainty in this number is, of course, quite large. As we pointed out in the previous section, this number is still less than that found by Butcher and Oemler (1985) and Dressler (1976). Thus, for example, if the true background density is 16 galaxies $\deg^{-2}$, we would expect to have found eight background objects in our spectroscopic sample. The probability of finding only three or fewer is just 4.2%. Fortunately, the cluster models we shall be deriving are quite insensitive to the background density. We shall return to the problem of background contamination in § VII*b*.

d) Search for Substructure

No subclustering is apparent in the galaxy distribution plotted in Figure 1. Our redshift data allow us to search for structure along the line of sight as well. Two cone diagrams are plotted in Figure 3, showing the galaxies projected along the major axis (p.a. = 120°) and the minor axis (p.a. = 30°) of the cluster. No clear separation of multiple components along the line of sight is seen. Thorough examination of the data in various velocity subsamples has similarly revealed no statistically compelling evidence for substructure. However, we note that we would be unable to detect substructure if the relative velocities of the components were 2500 km s^{-1} or less. If such a velocity separation were due to the Hubble flow alone, it would correspond to a spatial separation of 50 Mpc, more than an order of magnitude larger than typical cluster dimensions. The possibility of "hidden" substructure cannot be dismised lightly, given the high cluster velocity dispersion, the possibly non-Gaussian velocity histogram, and the elliptical morphology of the cluster.

IV. REVIEW OF X-RAY RESULTS

We briefly review the available X-ray data here; most of these results are drawn from FRG. A contour map of the 0.3–3.5 keV X-ray surface brightness of Abell 2256 obtained with the *Einstein Observatory* IPC is plotted in Figure 4*b* (Fig. 4*a* refers to a model described in § VII*c*). The map is background-subtracted, corrected for vignetting and other exposure variations, and smoothed to a resolution of 3′.5 FWHM. The X-ray emission is clearly elliptical with an axial ratio of about 1.2 and a mean position angle of about 120°; furthermore, the outer contours are not concentric with the emission peak but are offset to the southeast by about 2′. Otherwise, the emission is quite smooth. The emission peak occurs at $\alpha = 17^h6^m.9$, $\delta = 78°43'$ with an uncertainty of about 1′ in each coordinate.

Figure 5 is a plot of the azimuthally averaged X-ray surface brightness binned about the emission peak. The effective resolution for this profile is 1′.5 FWHM. A good analytic fit to radial profile (correcting for the finite resolution) is $S(r) \propto [1 + (r/5'.6)^2]^{-2}$. The allowed ranges (at 90% confidence) of the core radius and power-law exponent in this expression are also plotted. Assuming that the X-ray emissivity is proportional to the square of the gas density ν, the profile of gas density is then

$$\nu \propto [1 + (r/5'.6)^2]^{-1.25} . \quad (1)$$

The best-fit density profile and those allowed at the 90% confidence limits are plotted in Figure 6.

The high-energy cutoff of the *Einstein Observatory* mirror at 4 keV prevents an accurate measurement of the radial temperature distribution of the X-ray–emitting gas. Measurements of the integrated spectrum of the cluster with the *Ariel 5* satellite yield $kT = 7.7 \pm 1.0$ keV (Mitchell *et al.* 1979); *OSO 8* data give $kT = 7^{+3}_{-2}$ keV at 90% confidence (Mushotzky *et al.* 1978). Averaging the two results yields $7.4^{+1}_{-0.8}$ keV, where the errors are the 1 σ (68% confidence) limits. We find a total 0.2–4.0 X-ray luminosity of 1.1×10^{45} ergs s^{-1} and a central electron density of 2×10^{-3} cm^{-3}.

The cluster center determined from both the galaxy distribution and the X-ray map agree within 1′, with the optical center being northeast. The cluster center determined using Dressler's (1976) survey shifts progressively to the southwest by about 2′ as the limiting magnitude becomes fainter. Since error in each determination of the center is of order 1′, the X-ray and galaxy centers are consistent with each other. The galaxy counts are too sparse to search for a shift in the centroid of the isopleths of increasing radius as is seen in the X-ray map.

If the intracluster medium is in hydrostatic equilibrium in the cluster potential, then FRG show that the underlying cluster mass distribution must be considerably flatter than that of the gas. The apparent projected axial ratio a/b of the mass distribution must be of order 1.6 (averaged over radius), nearly independent of the true geometry of the mass distribution. The flattening of the galaxy distribution is not well determined (§ II*a*), with our survey giving 1.8 and Dressler's giving 2.3, but given the errors in these values they are compatible with the X-ray–determined value of 1.6. The range in position angle (114°–144°) of the galaxies is again entirely consistent with the X-ray position angle of 120°.

V. COMPARISON WITH THE COMA CLUSTER

Abell 2256 was selected for observation because it seemed to be closest in its properties to the Coma Cluster. It is of some interest to compare the two more closely. Abell 2256 is more distant than Coma by a factor of about 2.5, corresponding to a difference in distance modulus of 2.

a) Galaxy Density

From Kent and Gunn (1982), the Coma Cluster has 162 members to a blue limiting magnitude of 15.7 inside a radius of 95′. In Abell 2256 we estimate that there are 152 members (172 objects less 20 background) at our limiting red magnitude of 16.8 out to a comparable radius. Taking $B - r \approx 1$ for a typical galaxy, our limiting magnitude is equivalent to a blue magnitude of 17.8, slightly deeper than the comparable value for Coma. Therefore Abell 2256 has nearly the same number of galaxies as Coma.

b) Structure and Dynamics

Kent and Gunn (1982) find a core radius for the galaxy distribution in Coma of between 8′.5 and 10′.0; the corresponding range for Abell 2256 would be 3′.4–4′.0, in very close agreement with what we found in § II. The velocity dispersion of Abell 2256 is somewhat higher than that of Coma, about 1300 km s^{-1} versus 1068 km s^{-1} (when measured over a comparable range in radius); the difference is significant at the 97% confidence level. This leads to a larger mass estimate for Abell 2256 by a factor of 1.5.

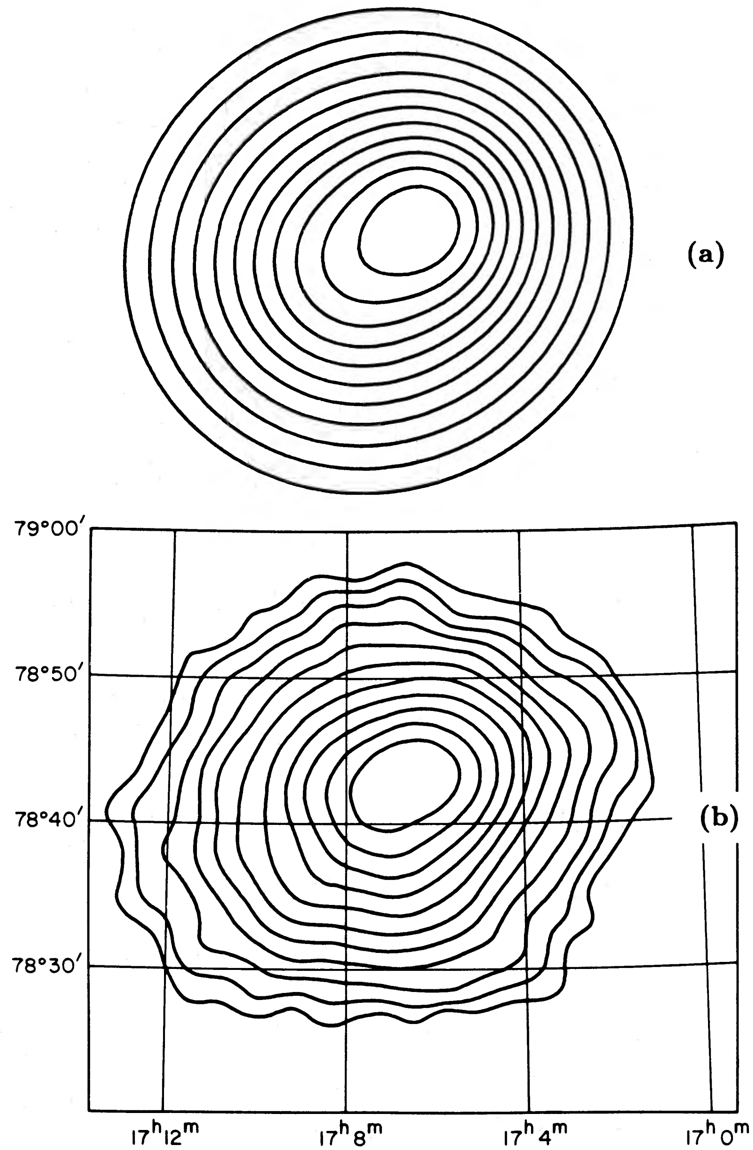

FIG. 4

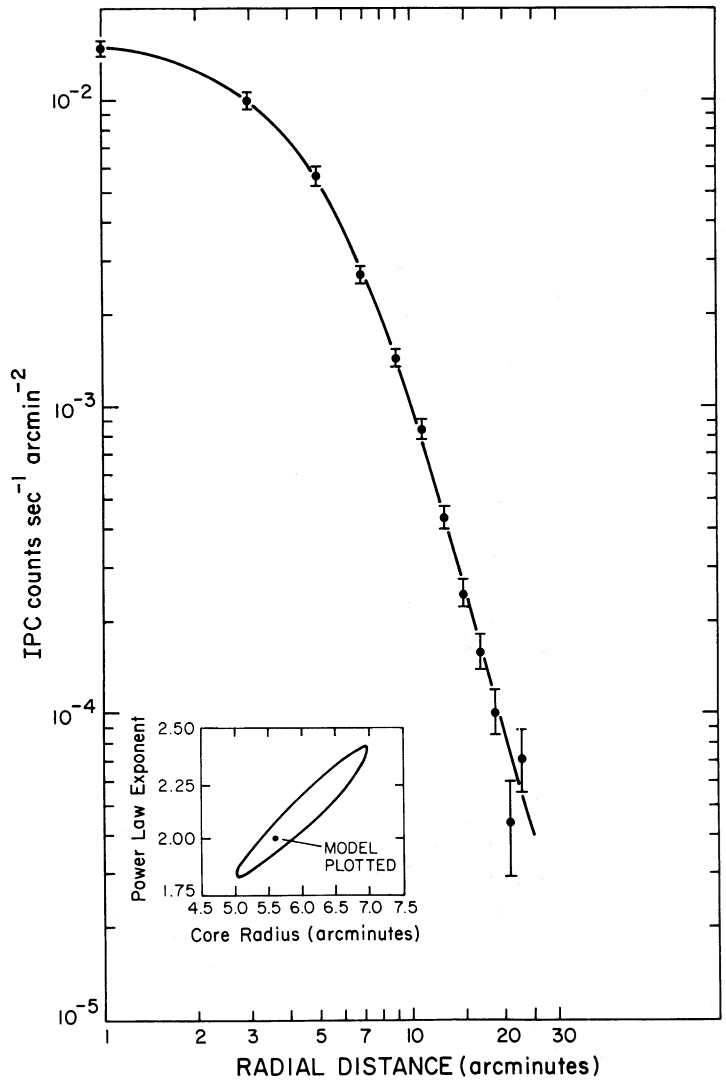

FIG. 5

FIG. 4.—(*a*) Contour plot of the X-ray surface brightness from the model described in § VII*e*. The map has been smoothed to a resolution of 3′.5 to facilitate comparison with the 0.3–3.5 keV map obtained with the *Einstein Observatory*, which is plotted below (*b*).

FIG. 5.—Azimuthally averaged X-ray surface brightness profile obtained with the *Einstein* IPC in the 0.3–3.5 keV band. The solid line is a fit to the profile of the form $S(r) \propto [1 + (r/5'.6)^2]^{-2}$, correcting for the IPC resolution of 1′.5 FWHM. The allowed range (at 90% confidence) of the core radius and power-law exponent in this fit are plotted in the inset.

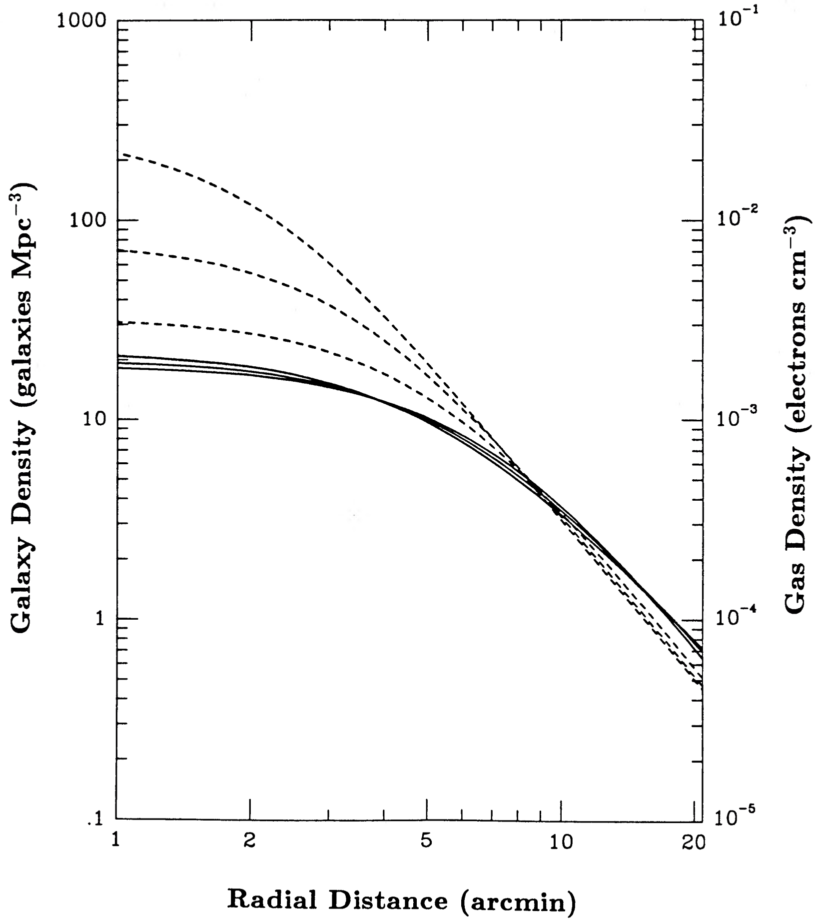

FIG. 6.—The (space) density profiles of the galaxies (*dashed lines*) and the X-ray–emitting gas (*solid lines*). Three curves are plotted for each quantity, representing the best fits to the data as well as the 90% confidence limits. The King model fits to the galaxy distribution are discussed in § IIc; the fits to the X-ray data are discussed in § IV.

c) X-Ray Properties

The X-ray properties of Coma are summarized by Mushotzky *et al.* (1978) and Abramopoulos, Chanan, and Ku (1981). Coma and Abell 2256 have quite similar luminosities, overall surface brightness profiles, central gas densities, and total gas masses. Both clusters contain gas at a temperature of about 8 keV, and both lack detectable cooling flows. The X-ray isophotes of both clusters are elliptical, with axial ratios of about 1.2, but are more nearly concentric in the case of Coma.

VI. RADIAL MASS DISTRIBUTION

Although a full treatment of the dynamics of Abell 2256 requires dealing with a flattened mass distribution, we are concerned primarily with the radial mass distribution and so will use spherically symmetric models. In § VII we consider the effects of flattening on the results.

a) Hydrostatic Equilibrium

A complete description of the dynamics of the galaxies and gas within the cluster requires six functions: the cluster mass distribution $M(r)$, the gas density and temperature profiles $\nu_{\rm gas}(r)$ and $T(r)$, the galaxy density profile $\nu_{\rm gal}(r)$, and the radial and tangential galaxy velocity dispersion profiles $\sigma_r(r)$ and $\sigma_t(r)$. Equivalently, we can replace $\sigma_t(r)$ with $\beta(r) = 1 - \sigma_t^2/\sigma_r^2$. A physically plausible model must have $\beta < 1$. These functions are constrained by four observables: the projected X-ray surface brightness and temperature profiles $S_x(r)$ and $T_x(r)$ and the projected galaxy density and velocity dispersion profiles $\mu_{\rm gal}(r)$ and $\sigma_p(r)$. In addition, the gas and galaxies individually must satisfy the equation of hydrostatic equilibrium and the ideal gas law:

$$\frac{k}{\mu}\frac{d(\nu_{\rm gas}T)}{dr} = -\frac{GM(r)}{r^2}\nu_{\rm gas}\,, \tag{2a}$$

$$\frac{d(\nu_{\rm gal}\sigma_r^2)}{dr} + \frac{2\beta\sigma_r^2\nu_{\rm gal}}{r} = -\frac{GM(r)}{r^2}\nu_{\rm gal}\,. \tag{2b}$$

Here $M(r)$ is the mass enclosed within a radius r, μ is the mean mass per gas particle [we use $\mu = 0.6m$(proton)], G is the gravitational constant, and k is Boltzmann's constant. In principle, these two equations combined with the four observables determine the cluster dynamics uniquely.

In practice, only the emission-weighted gas temperature is known, and the galaxy velocity dispersion profile is poorly constrained. Consequently, neither the optical nor the X-ray data alone or combined can be used to infer the mass distribution uniquely. In this section we show what constraints can be placed on the mass distribution as we impose and relax various assumptions.

The simplest assumptions that can be made about the gas and galaxy kinematics are that the gas is isothermal, the galaxy velocity dispersion is constant with radius, and the galaxy orbit distribution is isotropic (i.e., $\beta = 0$). However, we can show that these three assumptions are inconsistent with our data. If the galaxies and gas are at rest in a common gravitational potential, then their distributions are related via the equation of hydrostatic equilibrium and the ideal gas law, equation (2). We have

$$\frac{\mu\sigma_r^2}{kT}\left[\frac{d \ln \nu_{\rm gal}}{d \ln r} + 2\frac{d \ln \sigma_r^2}{d \ln r} + 2\beta\right] = \frac{d \ln \nu_{\rm gas}}{d \ln r} + \frac{d \ln T}{d \ln r} . \quad (3)$$

With the stated assumptions, we have

$$\frac{\mu\sigma^2}{kT} = \frac{d \ln \nu_{\rm gas}/d \ln r}{d \ln \nu_{\rm gal}/d \ln r} . \quad (4)$$

We have determined the slopes of the galaxy and gas density profiles at a radius of 15′; we pick this radius in order to be well outside the ill-determined cores of both profiles (Fig. 6). The slope of the galaxy density profile, taken from the best-fitting King model approximation in § II*b*, is -2.65; that of the gas density (from eq. [1]) is -2.20. These density profiles are compared in Figure 6. We also have estimated the average slope of the galaxy density profile by fitting a single power law to the profile given in Table 2, excluding all galaxies inside 5′; we find a slope of -2.62 with an error of ± 0.16. We use this error as an estimate of the uncertainty in the galaxy slope at 15′. The left-hand side of equation (4) is 1.43; the right-hand side is 0.83. By constructing joint χ^2 contours for both sides of this equation using our quoted errors, we find that the hypothesis of a consistent gravitational potential may be rejected with 99.3% confidence. Similar results are obtained if this comparison is made at a radius of 10′ or 20′. The sense of the discrepancy is that the optical data imply a greater cluster mass at 15′ than the X-ray data. Inconsistencies between optical and X-ray data of the same as we find for Abell 2256 have also been found for other clusters, most notably the Perseus Cluster (Gorenstein *et al.* 1978; Cowie, Henriksen, and Mushotzky 1987).

To proceed further, it is necessary to make some assumptions regarding either the mass, the temperature, or the anisotropy profiles. By specifying one we can determine (or at least constrain) the others by means of equation (2). We consider several possibilities.

b) *Mass Follows Light*

The simplest assumptions that can be made regarding the optical data are that the total cluster mass is distributed like the galaxies and the dynamics of both are described properly by the $W_0 = 8.5$ King model introduced in § II*c*. In this case the characteristic velocity dispersion of the King model is $\sigma_0 = 1435$ km s^{-1}. A plot of this fit is shown in Figure 7. With the limited data available the King model provides an entirely adequate description of the galaxy density and velocity dispersion profiles. The mass inside 20′ is $(2.2 \pm 0.3) \times 10^{15}$ $M_\odot$, with the error being dominated by the uncertainty in the velocity dispersion.

For a specified mass distribution and gas density profile, the gas temperature profile can be obtained by inverting equation (2a):

$$T(r) = \frac{1}{\nu(r)}\left[\nu_0 T_0 - \frac{\mu}{k}\int_0^r \frac{GM(r)}{r^2}\nu\, dr\right] . \quad (5)$$

One boundary condition, e.g., the central temperature, must be specified. Several gas temperature profiles corresponding to the mass distribution from the King model are plotted in Figure 8; the emission-weighted temperature is given in parentheses next to each curve. The emission-weighted temperature is an excellent approximation to the temperature obtained when isothermal models are fitted to the integrated spectra from more complex models (Fabricant 1978). At a minimum, the temperature must be positive at a radius of 20′; this sets a lower limit to the emission-weighted temperature of about 15 keV. If we define a parameter $\alpha = kT/\mu\sigma_0^2$, then the predicted value for α is 1.16, well in excess of the observed value $0.57^{+0.13}_{-0.10}$. (Although this parameter is commonly termed β elsewhere, we use α to avoid confusion with the anisotropy parameter.)

If the total mass profile has the same shape as the King model but the galaxy velocity distribution is anisotropic (i.e., $\beta \neq 0$), then the scale dispersion σ_0 of the King model will change. To compute $\beta(r)$ and σ_0, it is necessary to know the complete projected velocity dispersion profile. Somewhat arbitrarily, we assume that inside 20′ the projected velocity dispersion profile is the same as that given by the King model; outside 20′ we multiply the King model profile by a factor $20'/r^\eta$, where η is an exponent that is allowed to vary. This formulation allows us to mimic the behavior of the projected velocity dispersion profile seen in other clusters such as Coma (Kent and Gunn 1982), the Perseus Cluster (Kent and Sargent 1983), and Abell 2670 (Sharples, Ellis, and Gray 1988). Using the inversion equations given by Binney and Mamon (1982) and Tonry (1983), we have computed β and σ_r as a function of radius. For a given value of the exponent η, the total cluster mass (and hence σ_0) is fixed by the virial theorem. The maximum value for η (and hence minimum cluster mass) that produces a physical model ($\beta < 1$) is 0.45; the total cluster mass is 0.82 times that of the isotropic King model. The required emission-weighted gas temperature is then at least 12 keV, still inconsistent with the observed $7.4^{+1}_{-0.8}$ keV. Although the velocity dispersion profile is not constrained beyond a radius of 20′, given reasonable extrapolations, constant M/L ratio models cannot simultaneously match the X-ray and optical data.

c) *Polytropic Gas Models*

Merritt (1987) and The and White (1986) have both pointed out that if we relax the assumption that the mass follows the light, then there is a wide range of possible mass distributions that are consistent with a given set of projected galaxy density and velocity dispersion profiles. The X-ray data, however, restrict the range of possible models. Because we do not have a good measure of the full velocity dispersion profile, we have not explored a complete range of mass models. In this section we do explore a restricted set of models based on the assumption that the gas obeys a polytropic equation of state.

If the gas temperature profile were known, then the X-ray data could be used to determine the mass distribution uniquely. A common (although not necessarily correct) assumption is that the gas has a polytropic distribution: $T \propto \nu_{\rm gas}^{\gamma-1}$. By combining this relation with equations (1) and (2a), Cowie, Henriksen, and Mushotzky (1987) show that the mass profile is given by

$$M(r) = \frac{2kT_0 r_x \delta\gamma}{G\mu}\frac{x^3}{(1 + x^2)^{(1+\phi)}} . \quad (6)$$

In this equation, $x = r/r_x$, $\phi = \delta(\gamma - 1)$, T_0 is the central temperature, and r_x and δ are parameters describing the gas

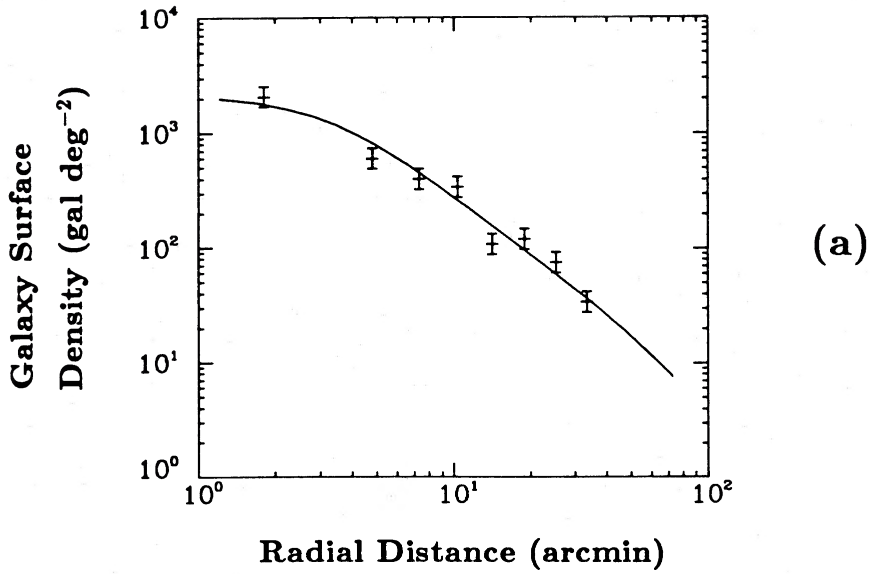

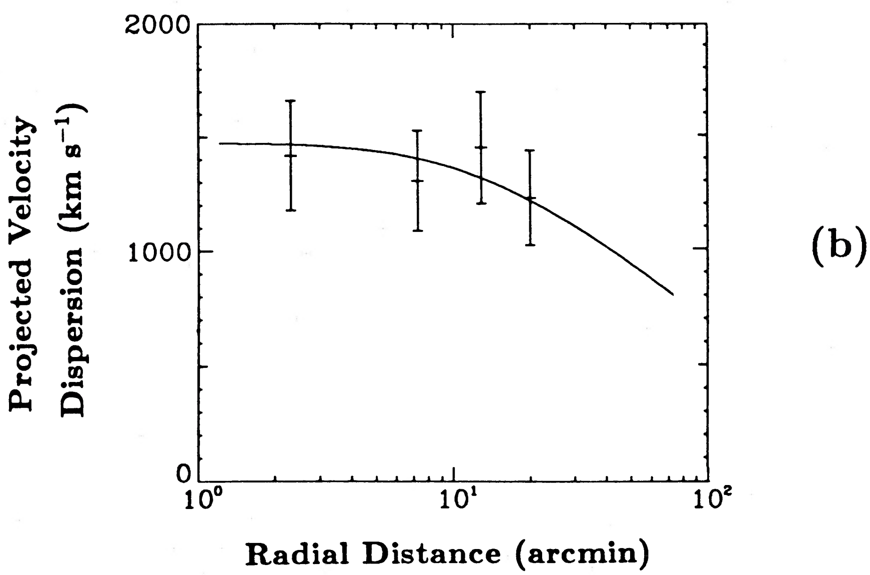

FIG. 7.—(*a*) Azimuthally averaged galaxy counts with a best-fitting King model (r_c = 3'.8, μ_0 = 2290 galaxies deg^{-2}, σ_0 = 1504 km s^{-1}). (*b*) The fit of the same model to the velocity data.

density profile (5.6 and 1.25, respectively, in eq. [1]). If we neglect the slow variation of emissivity with temperature, the emission-weighted temperature is related to the central temperature by

$$\langle T \rangle = T_0 \frac{\Gamma(2\delta + \phi - 3/2)\Gamma(2\delta)}{\Gamma(2\delta + \phi)\Gamma(2\delta - 3/2)} . \quad (7)$$

To determine which mass profiles are consistent with the optical data, we use the same approximations to the galaxy density and velocity dispersion profiles used in § VI*b* and again compute the radial dependence of σ_r and β. A dimensionless model is specified by the parameters γ, δ, r_x/r_c, and η. Because the galaxies are in virial equilibrium, the model predicts a specific value for the parameter α. A plausible model must reproduce the observed α within the observational errors and have $\beta < 1$.

Table 4 summarizes the results for a few different models. If the gas is isothermal ($\gamma = 1$), the lowest value of α that produces a physically realistic model is 0.70, a value that is within 1 σ of the best-fit value of 0.57. Models with a gas temperature decreasing with radius ($\gamma > 1$) rapidly become unacceptable; these models contain too little mass at large radii to bind the hot galaxy component. Models where the gas temperature increases mildly with radius ($\gamma < 1$) are acceptable; they have a

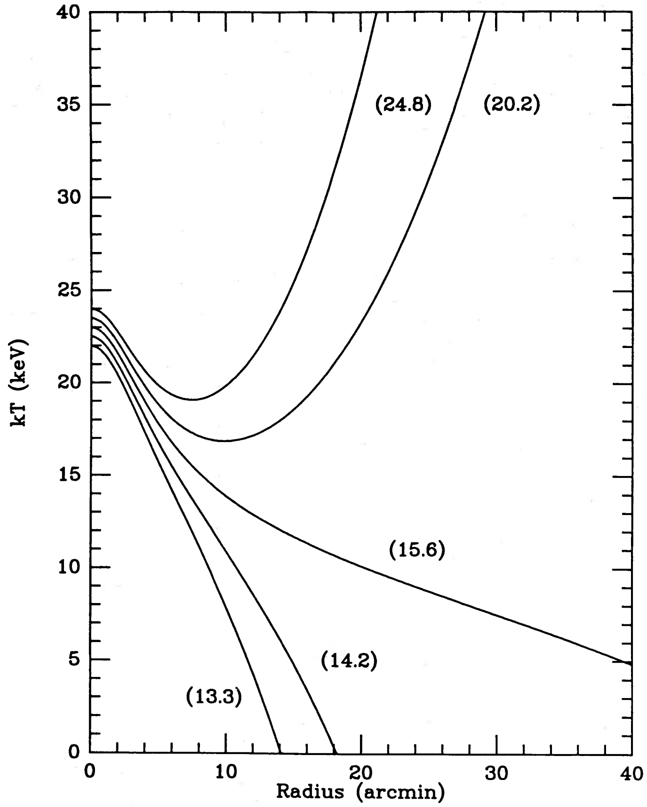

FIG. 8.—Series of possible X-ray temperature profiles that are consistent with the King model for the galaxies (with isotropic orbits) discussed in § VI*b*). The corresponding emission-weighted temperature is given in parentheses next to each curve. As discussed in the text, all of these profiles are inconsistent with the X-ray data.

mass profile that is more extended than either the galaxy or the gas distributions. These results are quite insensitive to moderate variations in r_x/r_c: varying the ratio between 1.0 and 1.8 changes the models insignificantly. In all cases the galaxy velocity distribution is isotropic in the center but very radially biased at large radii: in all cases between one-half and two-thirds of the kinetic energy is in radial motion, as compared with one-third for isotropic orbits.

VII. DISCUSSION

Our analysis thus far has assumed that the data suffer from no errors aside from statistical fluctuations and that the cluster is spherically symmetric. Although we have been able to find dynamical models that are consistent with both the optical and the X-ray data, these models have the properties that the cluster mass-to-light ratio increases with radius and that the galaxy motions are radially biased. These properties arise from

TABLE 4

PROPERTIES OF SAMPLE MASS MODELS

Model Type	γ	η	α	r_x/r_c
Mass follows light (not acceptable)	...	0.00	1.16	1.5
	...	0.45	0.93	1.5
Polytropic (acceptable)	1	0.15	0.70	1.5
	0.88	0.00	0.57	1.5
	1	0.18	0.65	1.0
	0.98	0.13	0.69	1.8

the fact that the equivalent gas velocity dispersion (kT/μ) is lower than the galaxy velocity dispersion, even though the gas has a flatter density profile. Next we examine alternative interpretations of the data that do not require radially increasing mass-to-light ratios and anisotropic galaxy orbits.

a) Peculiar Cluster Geometry

If the cluster is intrinsically triaxial, we need to consider the possibility that the cluster geometry has caused us to misinterpret the dynamics. In fact, we find that flattening is not likely to cause us to overestimate the cluster mass unless the cluster has an extreme geometry. Although detailed triaxial models for the cluster are quite complicated to construct, we can still study the global dynamical properties using the tensor virial theorem.

We first consider a spherically symmetric cluster with a density profile $\rho^*(\lambda)$, where $\lambda = r/r_0$ is a dimensionless radial coordinate and r_0 is some scale radius. We use the notation that starred quantities are what we compute assuming spherical symmetry; unstated quantities are the true values for the flattened cluster. Let the individual axes be scaled by factors a, b, c such that $\lambda^2 = (x/ar_0)^2 + (y/br_0)^2 + (z/cr_0)^2$, and the density profile in the new configuration has the same mass as the old: $\rho(\lambda) = \rho^*(\lambda)/(abc)$. The tensor virial theorem relates the potential and kinetic energies in the absence of rotation:

$$\Pi_{ij} + W_{ij} = 0 ,$$

where the kinetic energy tensor Π and potential energy tensor W are given by

$$\Pi_{ij} = \int \rho v_i v_j d^3x ,$$

$$W_{ij} = -\int \rho x_i \frac{\partial \Phi}{\partial x_j} d^3x . \quad (8)$$

For a triaxial ellipsoid with the coordinate system aligned along the principal axes, only the diagonal terms are nonzero. Binney (1978) shows that the potential energy tensor takes the form

$$W_{ii} = -\pi^2 G r_0^5 (a_i^2) a^2 b^2 c^2 A_i R , \quad (9)$$

where a_i is the scale length (a, b, or c) of axis i, A_i is a function of the axial ratios, and R is an integral of the density profile which, for our purposes, scales as the square of the density. In terms of the quantity R^* for the spherically symmetric case, we have $R = R^*/(abc)^2$. If we observe a cluster along one of its principal axes, we will observe a mean projected velocity dispersion $\langle \sigma_p^2 \rangle = -W_{ii}/M$, where M is the cluster mass. We wish to express W in terms of W^*, the quantity we compute incorrectly assuming spherical symmetry.

We do not know the intrinsic shape of Abell 2256. As two special cases, we consider an oblate spheroid viewed edge-on and a prolate spheroid viewed sideways. Let us view the cluster along the x-direction. In the first case, we have $a = b > c$, and A_x can be expressed in terms of elementary functions and $e = [1 - (c/a)^2]^{1/2}$:

$$A_x = \frac{1}{(r_0 a)^3 e} \left[\frac{1}{e^2} \arcsin e - \frac{(1 - e^2)^{1/2}}{e} \right] . \quad (10)$$

The projected axial ratio of the cluster is about 2 to 1. The galaxy data are binned in such a way that the scale factors obey $ac = 1$. Hence we have $a = 2^{1/2}$ and $c = 2^{-1/2}$. In the limit $e \to 0$, $A_x^* = 2/3r_0^3$. Then from equations (9) and (10), we have

$$W_{xx}^* = -\tfrac{2}{3}\pi^2 G R^* r_0^2 ,$$

$$W_{xx} = -0.666\pi^2 G R^* r_0^2 \approx W_{xx}^* .$$

Therefore, an oblate cluster seen edge-on will have the same projected velocity dispersion as a spherically symmetric cluster of the same mass.

For a prolate spheriod viewd sideways, $a > b = c$, and

$$A_x = \frac{1}{(r_0 a)^3 e^2}\left[\frac{1}{1-e^2} - \frac{1}{2e}\ln\left(\frac{1+e}{1-e}\right)\right]. \qquad (11)$$

We find $W_{xx} = 0.88 W_{xx}^*$. When viewed in this geometry, a prolate spheroid will have a lower projected velocity dispersion than a spherically symmetric cluster of the same mass.

Only if the cluster is more elongated along the line of sight than along either of the visible transverse axes will the assumption of spherical symmetry lead to a mass estimate that is too high. In this case the projected velocity dispersion is higher than a spherical cluster of the same mass. We have not performed the required triaxial calculations.

b) Background Contamination

A rather obvious explanation for the high cluster velocity dispersion is that there is an excess population of either foreground or background galaxies erroneously included as cluster members. For example, deleting 12 galaxies with $v > 19{,}000$ km s^{-1} would lower the cluster dispersion to 1080 km s^{-1}, approximately what is needed. Such a contamination would require a background with a density of 28 galaxies deg^{-2} in the narrow velocity interval $19{,}000 < v < 21{,}000$ km s^{-1}. This background density is larger than the *total* background that we used in § II, but since the distribution of galaxies is not uniform, such a high density may still be plausible. The velocity separation of the contaminants from the cluster mean must be $\sim$2000 km s^{-1}. If this velocity difference represents Hubble motion, then the separation would correspond to an angular separation of 6°–9° if projected on the plane of the sky. We do not have any good redshift surveys in this part of the sky to see whether the galaxy density near the cluster redshift is high enough.

In lieu of such a survey we refer to two well-studied regions: the region surrounding the Coma Cluster, and the Bootes void. The CfA redshift survey of the region around the Coma Cluster (de Lapparent, Geller, and Huchra 1986) shows several large, shell-like structures, including one in the velocity interval 2000–6000 km s^{-1} nearly projected onto the Coma Cluster. These structures may contaminate a cluster much more seriously than one would estimate if field galaxies were uniformly distributed. From data in Kent and Gunn (1982) we estimate that if the Coma Cluster were viewed from random directions, contamination comparable to what we observe in Abell 2256 would occur 4% of the time. Kirshner *et al.* (1987) find a density enhancement behind the Bootes void in the velocity interval $17{,}000 < v < 20{,}000$ km s^{-1} of 82 galaxies over 17.7 deg^2 to a limiting magnitude $V \approx 17.0$; these numbers yield a density of 4.6 galaxies deg^{-2}, falling short of what we require.

c) Superposition of Two Clumps

The high cluster velocity dispersion and its elliptical morphology can both be explained if there is substructure in Abell 2256, and we are viewing two superposed clumps aligned nearly along the line of sight. If this were the case, Abell 2256 would be similar to Abell 754 (Fabricant *et al.* 1986). We have therefore tried modeling the X-ray surface brightness map with the superposition of two spherically symmetric lumps, each containing isothermal gas at the same temperature with an X-ray surface brightness profile of the form $S(r) \propto [1 + (r/r_x)^2]^{-n}$. The free parameters then include the projected clump separation, the clump characteristic radii r_x, the exponent n (assumed to be the same for the two clumps), and the central surface brightness ratio of the two clumps. We have constrained this model by comparing the characteristics of the computed X-ray isophotes with those from the data tabulated in Table 2 of FRG. A total of 11 isophotes separated by a factor 1.5 in surface brightness were analyzed, comparing the surface brightness, the position of the isophote centers, and the axial ratio as a function of radius. The best-fitting model has clumps with core radii of 4'.3 and 6'.5 separated in projection by 5'.3. The power-law exponent is 2.1, and the central surface brightness of the smaller clump is 2.3 times that of the larger clump. Figure 9 compares the behavior of the isophotes for the model and data, and Figure 4*a* is a contour plot of the modeled surface brightness at 3'.5 resolution. For comparison, the observed surface brightness profile from FRG is plotted in Figure 4*b*.

The galaxy data are too coarse to permit any comparable modeling. However, we have verified that the galaxy distribution is consistent with the projected mass distribution inferred from the X-ray model. Treating the galaxies as identical test masses, we have applied the $V'/V'_{\max}$ test as described in Fabricant *et al.* (1986). We find that the X-ray model provides a completely acceptable description of the optical data. The velocity separation of the two clumps cannot be determined with any accuracy. The key point is that a large separation will lead to a large velocity dispersion for the composite system, while each clump individually has a much smaller dispersion. For example, two equal clumps each with an average dispersion of 990 km s^{-1} require a velocity separation of about 1700 km s^{-1} to reproduce the observed 1300 km s^{-1} of the combined system. Therefore,, such a model is completely consistent with all of the available data, and provides a natural explanation for the elliptical X-ray surface brightness profile and the elliptical galaxy surface density distributions as well.

The origin of the large velocity separation, however, would be difficult to understand. If it represents the Hubble expansion velocity between the two clumps, then the spatial separation must be of order 34 Mpc. In that case we must be fortunate in seeing two clumps (which are physically isolated clusters) so nearly aligned. If, on the other hand, the two clumps are infalling toward each other (due to their mutual gravitational attraction), then a rough calculation shows that they must be physically separated by less than about $5r_c$ in order to have such a large relative motion. In this case we must be viewing them at a very special time. The probability of either configuration occurring is difficult to calculate, in part because one reason Abell 2256 was selected for observation was precisely that it was known to have a high density of galaxies and a high velocity dispersion. Nevertheless, one can offer some support for either possibility. In the first case, clusters are themselves clustered (e.g., Bahcall and Soneira 1983; Postman, Huchra, and Geller 1986), so the probability of a chance alignment is greater than if clusters were distributed randomly. In the second case, numerical simulations show that cluster building is a continuous process of accretion of clumps, so at any time a given cluster is in the process of merging from smaller clumps.

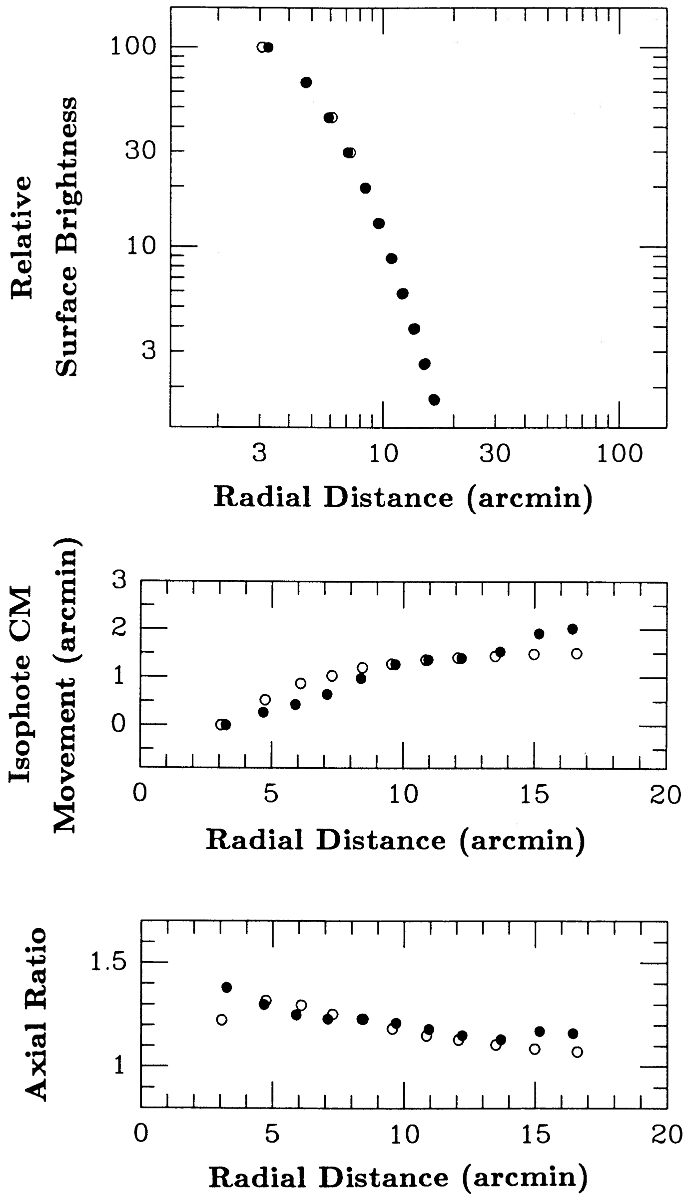

FIG. 9.—A detailed comparison between the X-ray data (*filled circles*, from Table 2 in FRG) and a two-clump model (*open circles*) as described in the text. The model has been smoothed to a resolution of 3$'$.5 for comparison with the data. The smaller but brighter clump is to the northwest. The model plotted has clumps with core radii of 4$'$.3 and 6$'$.5 separated by 5$'$.3. The central surface brightness of the smaller clump is 2.3 times that of the larger clump.

VIII. CONCLUSIONS

We find that the underlying mass distribution in Abell 2256 inferred from the galaxies, using a model in which the mass is distributed like the galaxies and the galaxy orbits are isotropic, is inconsistent with the X-ray data, in the sense that such a model implies more mass with a greater degree of central concentration. However, we do find a class of dynamical models for Abell 2256 that are consistent with the available X-ray and optical data. These models have the common features that the mass-to-light ratio increases with radius and that the galaxy orbits are anisotropic with a radial bias. These conditions can be avoided if the high galaxy velocity dispersion in Abell 2256 is the result of an extreme prolate geometry, high background contamination from galaxies with a redshift near that of Abell 2256, or the superposition of two clumps along the line of sight. In the last case, the ellipticity of the cluster seen in both the X-ray and the optical data may be simply the result of a superposition. Otherwise, the cluster must be intrinsically ellipsoidal as discussed in FRG.

Detailed comparisons of the optical and X-ray observations have been made for only a handful of other clusters, and the Coma Cluster is the only other comparable cluster with X-ray surface brightness observations of similar extent. For the Coma Cluster the X-ray and optical observations are more nearly compatible with a simple dynamical model of the type we reject for Abell 2256 (Hughes 1989; Cowie, Henriksen, and Mushotzky 1987; The and White 1987). The Perseus Cluster has a well-known discrepancy of the same sort we find for Abell 2256, namely, that the velocity dispersion of the galaxies is too high in comparison with the X-ray temperature (Gorenstein *et al.* 1978). However, the interpretation of the Perseus Cluster X-ray data is complicated by the presence of strong emission from cool gas surrounding NGC 1275, and a probable cooling flow (Fabian *et al.* 1981; Kent and Sargent 1983).

Our work with Abell 2256 (and previously Abell 754) underscores the potential of a unified treatment of the X-ray and optical results. The morphology of the X-ray emission and discrepancies in the distribution of the gas and galaxies provide important constraints on the cluster dynamics, even in the absence of a detailed knowledge of the temperature structure of the X-ray–emitting gas. That this should prove to be the case is ironic in view of the fact that Abell 2256 was originally chosen for study for its simplicity and symmetry.

We thank John Huchra for his valuable assistance in obtaining the optical spectra and Susan Tokarz for the reduction of the spectra. We also wish to thank Yoram Avni for assistance with statistical issues. D. F. acknowledges support from National Aeronautics and Space Administration grant NSG-5138. S. M. K. acknowledges support from National Science Foundation grant AST-84-51724. M. K. acknowledges support from NASA grant NAGW-201 and the Smithsonian Scholarly Studies Program.

REFERENCES

Abramopoulos, F., Chanan, G. A., and Ku, W. H. M. 1981, *Ap. J.*, **248**, 429.
Avin, Y. 1976, *Ap. J.*, **210**, 642.
Bahcall, N. A., and Soneira, R. M. 1983, *Ap. J.*, **270**, 20.
Binney, J. 1978, *M.N.R.A.S.*, **183**, 501.
Binney, J., and Mamon, G. 1982, *M.N.R.A.S.*, **200**, 361.
Butcher, H., and Oemler, A. 1985, *Ap. J. Suppl.*, **57**, 665.
Carter, D., and Metcalfe, N. 1980, *M.N.R.A.S.*, **191**, 325.
Cowie, L., Henriksen, M., and Mushotzky, R. 1987, *Ap. J.*, **317**, 593.
Davis, M., and Huchra, J. 1982, *Ap. J.*, **254**, 437.
de Lapparent, V., Geller, M., and Huchra, J. 1986, *Ap. J. (Letters)*, **302**, L1.
Dressler, A. 1976, Ph.D. thesis, University of California, Santa Cruz.
———. 1978, *Ap. J.*, **226**, 55.
Faber, S., and Dressler, A. 1977, *A.J.*, **82**, 187.
Fabian, A. C., Hu, E. M., Cowie, L. L., and Grindlay, J. 1981, *Ap. J.*, **248**, 47.
Fabricant, D. 1978, Ph.D. thesis, Harvard University.
Fabricant, D., Beers, T. C., Geller, M. J., Gorenstein, P., Huchra, J. P., and Kurtz, M. 1986, *Ap. J.*, **308**, 510.
Fabricant, D., Rybicki, G., and Gorenstein, P. 1984, *Ap. J.*, **286**, 186 (FRG).

Gorenstein, P., Fabricant, D., Topka, K., Harnden, F. R., and Tucker, W. H. 1978, *Ap. J.*, **224**, 718.
Harrison, E. R. 1974, *Ap. J.* (*Letters*), **191**, L52.
Hughes, J. P. 1989, *Ap. J.*, in press.
Kent, S. M. 1987, *A.J.*, **94**, 306.
Kent, S. M., and Gunn, J. E. 1982, *A.J.*, **87**, 945.
Kent, S. M., and Sargent, W. L. W. 1983, *A.J.*, **88**, 697.
Kirshner, R. P., Oemler, A., Schechter, P. L., and Shectman, S. A. 1987, *Ap. J.*, **314**, 493.
Kurtz, M. J., Huchra, J. P., Beers, T. C., Geller, M. J., Gioia, I. M., Maccacaro, T., Schild, R. E., and Stauffer, J. R. 1985, *A.J.*, **90**, 1665.
Latham, D. W. 1979, in *The MMT and the Future of Ground Based Astronomy*, ed. T. C. Weekes (*Smithsonian Ap. Obs. Spec. Rept., No. 385*), p. 119.
Merritt, D. 1987, *Ap. J.*, **313**, 121.
Mitchell, R., Dickens, R., Bell Burnell, S., and Culhane, J. 1979, *M.N.R.A.S.*, **189**, 329.
Mushotzky, R., Serlemitsos, P., Smith, B., Boldt, E., and Holt, S. 1978, *Ap. J.*, **225**, 21.
Oegerle, W. R., Hoessel, J. G., and Jewison, M. S. 1987, *A.J.*, **93**, 519.
Pearson, E. S., and Hartley, H. O. 1976, *Biometrika Tables for Statisticians*, Vol. **1** (London: Biometrika Trust), p. 67.
Postman, M., Huchra, J. P., and Geller, M. G. 1986, *A.J.*, **92**, 1238.
Sarazin, C. L. 1980, *Ap. J.*, **236**, 75.
Sharples, R. M., Ellis, R. S., and Gray, P. M. 1988, *M.N.R.A.S.*, **231**, 479.
The, L. S., and White, S. D. M. 1986, *A.J.*, **92**, 1248.
———. 1987, *A.J.*, **95**, 15.
Thuan, T. X., and Gunn, J. E. 1976, *Pub. A.S.P.*, **88**, 543.
Torny, J. 1983, *Ap. J.*, **266**, 56.
Tonry, J., and Davis, M. 1979, *A.J.*, **84**, 1511.

Daniel G. Fabricant, Stephen M. Kent, and Michael J. Kurtz: Harvard-Smithsonian Center for Astrophysics, 60 Garden Street, Cambridge, MA 02138